

1 **Revision 2**

2 **Near end-member shenzhuangite, NiFeS<sub>2</sub>, found in Muong Nong-type tektites from Laos**

3 Šárka Křížová<sup>1,2\*</sup>, Roman Skála<sup>1</sup>, Patricie Halodová<sup>3</sup>, Karel Žák<sup>1</sup>, Lukáš Ackerman<sup>1</sup>

4 <sup>1</sup> *Institute of Geology of the Czech Academy of Sciences, Rozvojová 269, CZ-165 00 Prague 6,*  
5 *Czech Republic*

6 <sup>2</sup> *Institute of Geochemistry, Mineralogy and Mineral Resources, Faculty of Science, Charles*  
7 *University, Albertov 6, CZ-128 43, Prague 2, Czech Republic*

8 <sup>3</sup> *Czech Geological Survey, Klárov 3, CZ-118 21 Prague 1, Czech Republic*

9

10

11 \*E-mail: [krizova@gli.cas.cz](mailto:krizova@gli.cas.cz)

12 **Abstract**

13 Australasian Muong Nong-type tektites from the locality centered at 16.46150° N, 106.48917° E  
14 in Laos contain sporadic spherical heterogeneous sulfide inclusions less than 10 μm in diameter,  
15 which have been identified by electron probe microanalyzer and electron back scatter diffraction  
16 to represent a mixture of rare mineral shenzhuangite with a pyrrhotite polytype (possibly troilite).  
17 Contrary to type shenzhuangite found in the shocked L6 chondrite Suizhou the mineral  
18 embedded in the tektite glass is nearly free of copper providing the composition close to its  
19 expected end-member not yet found in the nature; the empirical formula closest to ideal end-  
20 member composition based on 4 atoms per formula unit is Ni<sub>1.007</sub>Fe<sub>0.998</sub>Cu<sub>0.016</sub>Co<sub>0.058</sub>S<sub>1.922</sub>. The  
21 described occurrence also represents the first find of shenzhuangite in terrestrial material.

22 Presented is the Raman spectrum for shenzhuangite with tentative assignment of spectral bands  
23 based on the analogy with synthetic chalcopyrite-structured phases. The chemical composition of  
24 shenzhuangite close to  $\text{NiFeS}_2$  is not consistent with any stable phase in the Fe–Ni–S system up  
25 to melting temperature. Available data so far on phase relations in this system do not allow  
26 unambiguous interpretation of conditions under which sulfide association within inclusions had  
27 formed.

28 **Keywords:** shenzhuangite; tektites, Australasian strewn field; electron back scatter diffraction;  
29 electron probe microanalysis; Raman spectroscopy; meteoritic component

30

## 31 INTRODUCTION

32 Tektites are generally claimed to represent highly siliceous glassy products of hypervelocity  
33 impacts of extraterrestrial bodies on the Earth derived from the uppermost crustal unconsolidated  
34 rocks. They are commonly considered as distal ejecta of these high-energy events and occur in  
35 geographically well-defined areas called strewn fields (Koeberl 2014). The youngest and largest  
36 of these strewn fields is the Australasian field covering about 15% of the earth surface (Goderis  
37 et al. 2017; Folco et al. 2018). Among tektites, three major morphological types are recognized –  
38 splash-forms and Muong Nong-type tektites, and ablated forms. Small splash-forms sized below  
39 1 mm are called microtektites.

40 The Muong Nong-type tektites are commonly blocky, layered, and chemically more variable  
41 than splash-forms and enriched in volatile species (e.g.,  $\text{H}_2\text{O}$ , F, Cl, Bi, Sb; Koeberl 1992, 2014).  
42 They are also known to contain mineral inclusions, which may be relict phases that did not  
43 transform during the impact, or they can represent decomposition products or even newly formed

44 phases. Vast majority of these minerals, present as inclusions in tektite glass, are oxygen-bearing  
45 compounds (oxides, phosphates, silicates) and comprehensive data on them may be found in e.g.,  
46 Glass and Barlow (1979) and Cavosie et al. (2018). In addition to these inclusions, the so-called  
47 “metallic spherules” were reported from several Australasian tektites. The first note on metallic  
48 spherules comes from Chao et al. (1962). They found spherules consisting of dominant kamacite  
49 and minor troilite and phosphide in tektites from Isabela on Luzon, Philippine Islands. In the  
50 further paper, Chao et al. (1964) report on finds of metallic inclusions in Australasian tektites  
51 from Ortigas site on Luzon (The Philippines) and Dalat in Vietnam. Beside kamacite and troilite  
52 (up to 5 vol%), they unambiguously identified schreibersite ((Fe,Ni)<sub>3</sub>P attaining the content of up  
53 to 35 vol%). The inclusions were either spherical or elliptical and range from a few micrometers  
54 to 800 μm across, with most of them being sized > 100 μm. Similar, yet smaller inclusions have  
55 been reported from impact glasses of several impact craters worldwide (e.g., Aouelloul,  
56 Barringer, Bosumtwi, Wabar; see Chao et al., 1966; El Goresy, 1966; Brett, 1967 and references  
57 therein). Mineral composition of the inclusions consisting of kamacite ± troilite ± schreibersite  
58 was by most considered to be a proof of their meteoritic origin. However, Ganapathy and  
59 Larimer (1983) and O’Keefe (1984) claimed that the meteoritic origin of inclusions is not  
60 supported by the results of chemical analyses. In the course of study of Muong Nong-type  
61 Australasian tektites from Laos, we found small (less than 10 μm in diameter) purely sulfide  
62 spherules, which display chemical composition close to NiFeS<sub>2</sub>. Such composition resembles  
63 that of the end-member of the recently described chalcopyrite-structured mineral shenzhuangite  
64 (empirical formula  $^{[4]}(\text{Ni}^{2+}_{0.69}\text{Cu}^{+}_{0.31})^{[4]}(\text{Fe}^{2+}_{0.69}\text{Fe}^{3+}_{0.31})^{[6]}\text{S}_{2.00}$ ) found in the shocked L6 chondrite  
65 Suizhou (Bindi and Xie 2018).

66 The purpose of this paper is to characterize the NiFeS<sub>2</sub> phase assemblage found in Laotian  
67 tektites to test its identity with previously described mineral shenzhuangite and discuss the origin  
68 of the Fe–Ni sulfide spherules in tektite glass.

69

## 70 **SAMPLES AND EXPERIMENTAL TECHNIQUES**

71 Forty-seven polished thin sections were prepared from 31 samples of Muong Nong-type tektites  
72 collected during our fieldwork at different locations in Laos. One to three polished thin sections  
73 (~400 μm thick) were prepared from each specimen. Rare sulfide inclusions containing NiFeS<sub>2</sub>  
74 phase were identified only in samples found at the single locality east of a local main road about  
75 10 km north of the village Muong Nong (GPS coordinates 16.46150° N, 106.48917° E; see Žák  
76 et al. 2019). Sixteen thin sections were prepared from 12 samples of Muong Nong-type tektites  
77 from this locality and studied in detail. The inclusions of shenzhuanite were found only in four  
78 samples (MN 7, MN 12, MN 13 and MN 16). The macroscopic appearance and the photographs  
79 of the thin section of the samples MN 12, MN 13, and MN 16 are shown in Fig 1. The sample  
80 MN 7 is imaged in Žák et al. (2019). Overall, only 6 inclusions exceeding the diameter of ~5 μm  
81 allowing their unambiguous identification as shenzhuangite were observed in five thin section.

82 Optical polarization microscope Olympus BX 51 was used for preliminary characterization of  
83 the spherules and their mutual relationships with hosting glass. Scanning electron microscope  
84 Tescan VEGA3XMU (Department of Analytical Methods, Institute of Geology of the Czech  
85 Academy of Sciences, Prague) was used to screen tektites with back-scattered electron imaging  
86 as well as to obtain semiquantitative analyses with an energy-dispersive spectrometer Bruker  
87 X'Flash 5010.

88 Electron microprobe analyses of sulfide inclusions were carried out using a CAMECA SX-100  
89 electron microprobe equipped with four wavelength-dispersive X-ray spectrometers (WDS) at  
90 the Institute of Geology of the Czech Academy of Sciences in Prague. The operating conditions  
91 to analyze sulfide inclusions were 15 kV accelerating voltage, 10 nA beam current, focused  
92 electron beam and counting times 20 s for peak and 10 s for background. The following elements  
93 were analyzed using their  $K\alpha$  spectrum lines (standard, spectrometer crystal, and detection limit,  
94 respectively, are given in parentheses): Fe (hematite, LLIF, 1400 ppm), Mn (rhodonite, LLIF,  
95 1700 ppm), Co (cobalt, LLIF, 1700 ppm), Ni (nickel, LLIF, 1400 ppm), Cr (chromium, LLIF,  
96 1000 ppm), Cu (copper, LLIF, 2000 ppm). The X-phi (Merlet, 1992) correction procedure was  
97 used to process the measured data. The accuracy of analyses is 5 rel% or better for each element.  
98 Major element compositions of tektite glass surrounding the inclusions were also obtained by  
99 electron microprobe (EPMA) CAMECA SX-100. A loss of volatile elements has been  
100 prevented by using defocused electron beam (diameter 2  $\mu\text{m}$ ) and a sample current of 4 nA the  
101 accelerating voltage was 15 kV. Analyses followed the protocol given in Jonášová et al. (2016)  
102 and Skála et al. (2016).

103 Identification of the crystal structure type for individual inclusions and/or their parts was  
104 performed through electron backscatter diffraction (EBSD). Before the EBSD examination,  
105 surfaces of the thin section were polished using a colloidal silica suspension (OP-U, Struers).  
106 The electron backscatter patterns (EBSP) were obtained using a Tescan MIRA 3GMU scanning  
107 electron microscope equipped with NordlysNano (Oxford Instruments) detector housed at the  
108 Czech Geological Survey, Prague. For EBSP collection, the FEG-SEM was operated at an  
109 accelerating voltage of 20 kV, with the thin section tilted at an angle of  $70^\circ$  to the beam, and at a  
110 working distance of 20 mm. The obtained EBSPs were processed and indexed using AZtec

111 acquisition software. For the phase identification, the collected EBSPs were matched with  
112 simulated diffraction patterns determined from candidate phases based on crystal structure data  
113 for shenzhuangite (Bindi and Xie 2018), troilite (Keller-Besrest and Collin 1990), pyrrhotite 1C  
114 (ICSD code 29301; Bergerhoff and Brown 1987), cubanite (ICSD code 53263; Bergerhoff and  
115 Brown 1987) and pentlandite (Rajamani and Prewitt 1975).

116 To supplement structural information on Fe-Ni sulfide spherules, a Raman microspectrometer  
117 S&I MonoVista CRS+ was used (Institute of Geology of the Czech Academy of Sciences in  
118 Prague). The system is based on Princeton Instruments SP2750i spectrometer with a focal length  
119 of 750 mm and a CCD detector Andor iDus 416. Laser beam was focused on a sample with a  
120 100× magnifying objective (providing ~1 μm lateral resolution) attached to an Olympus BX  
121 51WI microscope. The spectra were obtained in back-scattered geometry. The accuracy of the  
122 wavenumber axis was calibrated with an Intellical Hg-Ne/Ar lamp (Princeton Instruments). The  
123 system was calibrated with a silicon standard. Raman spectra were excited with a laser of  
124 nominal 532 nm wavelength and power at the sample surface was about 2.5 mW to prevent  
125 sample deterioration that is known to occur in Raman experiments involving natural sulfides, see  
126 discussion by Weber et al. (2017). Spectra were acquired with a grating of 1200 gr/mm density.  
127 Band positions and other profile parameters have been fitted with Fityk software (Wojdyr 2010).

## 128 **RESULTS**

129 Two-phase sulfide inclusions of spherical shape less than 10 μm in diameter occur in the Muong  
130 Nong-type tektites recovered from a large tektite body close to Muong Nong village. They were  
131 found in portions of tektite glass, which is substantially vesiculated. The bubbles are usually  
132 spherically shaped and their diameter varies in broad range from less than 10 μm to as much as  
133 400 μm. The glass is finely layered in the transmitted light inoptical microscope. The lighter

134 schlieren and patches are of yellowish color whereas darker ones are brownish-colored.  
135 Lechatelierite (pure silica glass) filaments have also been noticed in the glass (Fig. 2). In BSE  
136 images, the glass highlighting its finely layered structure immediately surrounding the spherules  
137 is light gray usually irregularly crosscut by vermiform darker features of thickness less than 5  
138  $\mu\text{m}$  and tens to hundreds of  $\mu\text{m}$  in length. Chemical composition of tektite glass of five thin  
139 sections hosting the inclusions immediately in the inclusion surroundings is relatively uniform  
140 varying between following limits (in wt%):  $\text{SiO}_2$  73.0–75.5,  $\text{TiO}_2$  0.70–0.76,  $\text{Al}_2\text{O}_3$  11.9–12.7,  
141  $\text{FeO}$  4.14–4.66,  $\text{MgO}$  1.71–2.07,  $\text{CaO}$  1.31–2.33,  $\text{Na}_2\text{O}$  1.54–1.84, and  $\text{K}_2\text{O}$  2.41–2.58.  
142 All the inclusions display sharp contacts with the host tektite glass. In some cases, a few fine  
143 protrusions radiate to a surrounding glass from the surface of inclusions; the length of  
144 protrusions is well below 10 rel% of inclusion diameter, however, in most cases this proportion  
145 is less than 5 rel% (Fig. 3). All discovered Fe–Ni–S inclusions are chemically heterogeneous  
146 consisting essentially of two well spatially separated phases, which differ in Ni content. Mutual  
147 proportions of Fe–Ni–S and Ni-bearing Fe–S phases are variable from one inclusion to the other.  
148 The distribution of the phases within spherules has either patchy or segmented appearance. The  
149 former type of inclusion is illustrated in the BSE image in Fig. 3 b while the latter is shown in  
150 Fig. 3c.  
151 Crystal structure type of both minerals forming the inclusions has been identified from 8 Kikuchi  
152 bands in EBSP taken from parts seemingly homogeneous in BSE. The lowest values of the mean  
153 angular deviation (MAD) representing the misfit value of the indexing of a measured EBSP from  
154 the pattern calculated for given match unit were  $0.42^\circ$  for Ni-richer phase and  $0.46^\circ$  for Ni-  
155 poorer phase, respectively. Since the values  $\text{MAD} < 1^\circ$  are considered as indicators of good fit,  
156 the Ni-richer phase may be unambiguously identified as shenzhuangite (Fig. 4) while the Ni-

157 poorer phase correspond to troilite. It should be noted, however, that other ordered pyrrhotite  
158 polytypes with low number of stacking layers (e.g. 1C) used as match units provided similar  
159 MAD values making the identification of the Ni-poorer phase less reliable.

160 The chemical composition of Fe–Ni–S inclusions vary considerably, nevertheless, two mineral  
161 phases are clearly defined. Mineral structurally corresponding to shenzhuangite contains  
162 typically more than 23 at% Ni. Nickel contents in troilite/pyrrhotite phase vary in the range from  
163 0.2 to 8.9 at% possibly representing an analytical artefact due to intimate intergrowths of Ni-free  
164 troilite/pyrrhotite with shenzhuangite. Shenzhuangite contains also up to 1.5 at% Co. All  
165 shenzhuangite analyses are slightly sulfur-deficient, the mineral contains between 46.8 to 49.7  
166 at% S. Complete results of EPMA analyses of shenzhuangite are summarized in Table 1 and  
167 shown in Fe–Ni–S plot (Fig. 5). Totals of almost all analyses are below 98 wt% due to small size  
168 of the spherules, which also means that their thickness is low so the electron beam penetrates the  
169 complete volume of the inclusion and hits the glass below; this feature was explained for  
170 complex metallic-sulfide spherule inclusions described from the glass of the Bosumtwi crater by  
171 El Goresy (1966). Consequently, we decided to neglect other elements otherwise present solely  
172 in glass, which were observed only at very low contents, and to normalize the analytical data in  
173 Table 1 to 100 wt%.

174 The Raman spectrum of shenzhuangite (Fig. 6) displays the prominent bands at 288, 370, and  
175 390  $\text{cm}^{-1}$ . In addition to them, there are several weaker further unresolved bands and shoulders to  
176 the main bands. Results of the fitting of the Raman spectrum are summarized in Table 2. It  
177 should be also noted that despite the relatively long overall counting time the signal-to-noise  
178 ratio for shenzhuangite Raman spectrum is worse than that for the isostructural chalcopyrite

179 taken under the same spectrum acquisition conditions. The Raman spectra of chalcopyrite and  
180 pentlandite are shown in Fig. 6 for comparison with spectrum of shenzhuangite.

181

## 182 **DISCUSSION**

183 The inclusions found in vesiculated glass of tektite samples found close to Muong Nong village  
184 in Laos are, contrary to so far known spherules from Australasian tektites, completely devoid of  
185 pure metal, which was a substantial portion of the so-called “metallic spherules” described by  
186 Chao et al. (1962, 1964) from philippinites and indochinites. The inclusions described by Chao  
187 et al. (1962, 1964) contain next to kamacite also troilite and/or schreibersite; the latter mineral  
188 was not found in the studied inclusions in Laotian Muong Nong-type tektites. Clearly, the  
189 inclusions in studied Muong Nong-type Australasian tektites represent a new chemical type of  
190 inclusions in the tektite glass consisting solely of sulfides. In addition, they are much smaller  
191 (less than 10  $\mu\text{m}$  across) than the metallic spherules from splash-form tektites that typically  
192 exceed 100  $\mu\text{m}$  in diameter. Obviously, both types of inclusions formed under different  
193 conditions and reflect different character of both tektite types.

194 Refinement of the crystal structure of shenzhuangite carried out by Bindi and Xie (2018) showed  
195 that chalcopyrite and shenzhuangite are isostructural. Chalcopyrite-structured phases crystallize  
196 in the space group  $I\bar{4}2d$ . In the end-member chalcopyrite,  $\text{Cu}^+$  is located in the tetrahedrally  
197 coordinated site  $4a$  while  $\text{Fe}^{3+}$  is in tetrahedrally coordinated  $4b$  site and  $\text{S}^{2-}$  in the  $8d$  site (Hall  
198 and Stewart 1973). Distribution of valences for Cu and Fe in chalcopyrite was confirmed by  
199 several experimental and theoretical studies (e.g., Boekema et al., 2004; Goh et al., 2006;  
200 Klekovkina et al., 2014). Taking into account the chemical composition of shenzhuangite from  
201 the Suizhou chondrite, Bindi and Xie (2018) suggested a mixed ( $\text{Cu}^+ + \text{Ni}^{2+}$ ) occupancy in site  $4a$ .

202 To keep the mineral electroneutral, introduction of ferrous iron to structure is required, hence the  
203 site *4b* shows a mixed occupancy of ( $\text{Fe}^{2+} + \text{Fe}^{3+}$ ) type. They, however, admitted also the  
204 possibility of atom partitioning over the structure sites following the formula  
205  $(\text{Ni}^{2+}_{0.69}\text{Fe}^{2+}_{0.31})(\text{Fe}^{2+}_{0.38}\text{Fe}^{3+}_{0.31}\text{Cu}^{+}_{0.31})\text{S}_2$ , which would better fit the trend in the distribution of  
206 cations over the two structure sites based on their ionic radii. Since chalcopyrite structure may be  
207 derived from the sphalerite-based archetype structure, we applied the Vegard rule otherwise most  
208 appropriated for cubic lattices to estimate the crystal structure of the end-member shenzhuangite  
209 found in our Muong Nong-type Australasian tektites. The model with Ni occupying *4a* site and  
210 Fe completely located in *4b* site was adopted. An extrapolation of the data for end-member  
211 chalcopyrite (Hall and Stewart, 1973) and published shenzhuangite structure (Bindi and Xie  
212 2018) provides following unit-cell dimensions  $a = 5.3225 \text{ \AA}$ ,  $c = 10.502 \text{ \AA}$ ,  $V = 297.48 \text{ \AA}^3$  and  
213 distances Ni-S of  $2.260 \text{ \AA}$  and Fe-S of  $2.328 \text{ \AA}$ , respectively. Then, the distances has been used  
214 to estimate the fractional coordinate of sulfur atom in *8d* site using the quantity of tetragonal  
215 distortion defined in, e.g., Camassel et al. (1990) or Mintairov et al. (1999), as  $x_S = 0.2390$ .

216 To provide an independent insight to the crystal structure of shenzhuangite, we applied the  
217 Raman microspectroscopy. Since chalcopyrite-structured phases of  $\text{A}^{\text{I}}\text{B}^{\text{III}}\text{C}^{\text{VI}}_2$  and  $\text{A}^{\text{II}}\text{B}^{\text{IV}}\text{C}^{\text{V}}_2$   
218 types often display semiconducting properties and/or they are used as photovoltaic or nonlinear-  
219 optical materials (Mintairov et al. 1999), there is a wealth of dedicated Raman and lattice  
220 dynamics studies of these phases (e.g., van der Ziel et al. 1974; Artus et al. 1990; Camassel et al.  
221 1990; Ohrendorf and Haeuseler 1999a, 1999b and references therein). Unfortunately, only few  
222 studies have been focused at least in part on the chalcopyrite *sensu stricto* (e.g., Koschel et al.  
223 1975; Ohrendorf and Haeuseler 1999a; Łażewski et al. 2004). That makes the interpretation of  
224 the spectra of shenzhuangite rather ambiguous. In addition, as far as we know there are no

225 Raman data available for chalcopyrite-structured phase of general formula  $A^{II}B^{II}C^{VI}_2$  which  
226 further markedly complicates the assignment of the Raman bands.

227 In general, the total number of Raman-active optic modes that can be observed in the Raman  
228 spectra of chalcopyrite-structured phases is seventeen:  $1A_1(\Gamma_1)+3B_1(\Gamma_3)+2B_2(\Gamma_4)(TO)+$   
229  $2B_2(\Gamma_4)(LO) + 1B_2(\Gamma_4)(LO + TO)+ 2E(\Gamma_5)(TO)+ 2E(\Gamma_5)(LO)+ 4E(\Gamma_5)(LO + TO)$ , where  $(LO +$   
230  $TO)$  indicates an unsplit polar mode; atop of the optic modes there are 2 acoustic modes  $(1B_2 +$   
231  $E)$  (Kaminow et al. 1970; Mintairov et al. 1999; Huang et al. 2016). To test the possibility to  
232 assign Raman bands in the spectrum of shenzhuangite, we compared it to the Raman spectrum of  
233 natural chalcopyrite taken from the RRUFF database (R050222; Lafuente et al., 2015) that we  
234 processed in the same way as we did for shenzhuangite. The most prominent band in the Raman  
235 spectrum of chalcopyrite is an asymmetric feature consisting of two overlapping peaks centered  
236 at 286 and 291  $\text{cm}^{-1}$  with half-widths of 10 and 5  $\text{cm}^{-1}$ , respectively (Fig. 6). The position of  
237 higher and narrower peak at 286  $\text{cm}^{-1}$  is consistent with  $A_1$  mode (e.g., Łażewski et al., 2004),  
238 which is the most intensive band in many chalcopyrite-structured synthetic materials. In  
239 shenzhuangite Raman spectrum, however, the most intensive band occurs at 370  $\text{cm}^{-1}$  which  
240 value coincides with the peak corresponding to  $E(LO)$  and  $B_2(LO)$  modes of chalcopyrite  
241 spectrum with only ca 6 % relative intensity. Pentlandite spectrum (RRUFF database entry  
242 R060144) is incompatible with both shenzhuangite and chalcopyrite spectra precluding its  
243 presence in the inclusions.

244 Since studies of synthetic chalcopyrite-structured phases showed sphalerite structure as useful  
245 archetype to interpret Raman spectra of the former materials, we inspected published data  
246 investigating the role of impurities on sphalerite Raman spectra. Influence of transitional metals,  
247 in most cases iron, contents in sphalerite on the position of Raman bands and their intensities has

248 been assessed by Zigone et al. (1981), Jiménez-Sandoval et al. (2003), Kharbish (2007),  
249 Osadchii and Gorbaty (2010) and Buzatu et al. (2013). They observed shift of Raman band  
250 positions, emergence of new peaks as well as changes in mutual intensity ratios between  
251 individual peaks. Zigone et al. (1981) noticed systematic shift of  $A_1$  mode from 303 to 293  $\text{cm}^{-1}$   
252 for ~1 % admixture of transient metals from Ni to Cr; obviously, an introduction of lighter  
253 element to sphalerite structure results to shift of the Raman band to lower wavenumbers.  
254 Generalizing these observations to chalcopyrite-type structures allowed consideration of the role  
255 of the change of atomic masses, force constants and structural distortions on the Raman band  
256 positions, intensities and percentages of atomic contribution to individual Raman-active modes  
257 (Artus et al. 1990; Pascual et al. 1991). Developed concept of alternating anion-cation bond  
258 strength (Pascual et al. 1991) allows explanation of the differences between chalcopyrite and  
259 shenzhuangite in terms of ~8 rel. % change in atomic mass at the structure site  $4a$ , lengthening  
260 cation-anion distance within the tetrahedron occupied by Fe while the distances involving Ni and  
261 S shorten in comparison with those for equivalent structure sites in chalcopyrite. In addition,  
262 local force variation may be also expected due to change in  $3d$ -electron configuration ( $\text{Ni}^{2+} 3d^8$   
263 and  $\text{Fe}^{2+} 3d^6$  in shenzhuangite vs.  $\text{Cu}^+ 3d^{10}$  and  $\text{Fe}^{3+} 3d^5$  in chalcopyrite). As a consequence,  
264 modes involving Ni–S vibrations will harden and shifts up while those reflecting Fe–S  
265 displacements will soften and shifts down. The tentative assignment of the Raman band mode  
266 symmetries based on crude estimate of analogies with natural chalcopyrite and synthetic  
267 chalcopyrite-structured phases of similar atomic mass ratios is provided in Table 2. The mode  $A_1$   
268 reflects solely vibrations of anionic part of the structure while other modes are due combined  
269 displacements of cations and anions, which mutually influence each other making

270 straightforward unambiguous mode assignment impossible (Kaminow et al. 1970; Artus et al.  
271 1990; Artús et al. 1991; Mintairov et al. 1999; Huang et al. 2016).

272 Worse quality in terms of signal-to-noise ratio of the shenzhuangite Raman spectrum than that of  
273 isostructural chalcopyrite is most probably due to defects of the crystal structure. Possible  
274 reasons why these defects were introduced to the structure may involve undercooling resulting in  
275 slight positional disorder or lattice strain developed along interfaces with pyrrhotite/troilite  
276 domains.

277 Bindi and Xie (2018) described shenzhuangite from Suizhou L6 meteorite. It occurs in  
278 immediate association with taenite. In the Fe–Ni–Cu–S system under terrestrial conditions, no  
279 stable phase of the composition they measured for shenzhuangite is known. Consequently, they  
280 hypothesized that the mineral formed as a product of sulfurization of taenite under specific  
281  $pS_2/pO_2$  ratio. Since no sulfur has been reported in any study of chemical composition of  
282 Australasian tektites (see Glass and Barlow 1979; Koeberl 1992, 2014 and references therein),  
283 the process of sulfurization as suggested by Bindi and Xie (2018) cannot be adopted to explain  
284 the origin of shenzhuangite in Muong Nong-type Australasian tektites.

285 Chemical composition of shenzhuangite found in inclusions in a tektite glass plot in the Fe–Ni–S  
286 system (Fig. 5) near a region of monosulfide solid solution + liquid, monosulfide solid solution +  
287 high-form pentlandite + liquid or monosulfide solid solution + high-form pentlandite fields in  
288 isothermal sections at 875, 850, and 800 °C, respectively (Kitakaze and Sugaki 2004; Kitakaze et  
289 al. 2011, 2016). Previous study on phase relations in a system Fe–Ni–Co–S by Kitakaze and  
290 Sugaki (2004) quotes the melting temperature for  $Fe_{4.5}Ni_{4.5}S_8$  as 982 °C. Although the bulk  
291 chemical composition of the spherules is hard to ascertain due to variable proportions of  
292 shenzhuangite and troilite/pyrrhotite, that temperature still provides a reasonable constraint on

293 the potential cooling history of the inclusions. Obviously, they have to be quenched in a narrow  
294 range between ca 1000 °C and 900 °C. Origin and time of crystallization of pyrrhotite/troilite  
295 phase is questionable, it can crystallize simultaneously with shenzhuangite directly from an  
296 initial sulfide melt, which was enriched in Fe compared to the composition of shenzhuangite, or  
297 it may exsolve later in subsolidus. Tektite glass immediately surrounding the shenzhuangite-  
298 troilite inclusions lacks radial fractures and the spherules occasionally display the cusp  
299 protrusions intruding to the glass. This feature seems to be compatible with concomitant  
300 solidification of tektite glass and crystallization of sulfide inclusions. The diameters of observed  
301 inclusions do not exceed 10 μm and this size is small enough to keep them spherical since the  
302 surface tension predominates over body forces under such conditions (Barnes et al. 2017).

303 The origin of sulfur and nickel to form described sulfide inclusions is uncertain, yet principally  
304 only two sources represent a viable explanation. Either the parentage is purely terrestrial and  
305 sulfides with unstable chemical composition formed due to thermodynamically unequilibrated  
306 conditions at high temperatures and pressures associated with highly reducing conditions ruling  
307 during the impact of the extraterrestrial body or the inclusions may represent an extraterrestrial  
308 matter derived from a projectile that were in some way incorporated to the tektite glass. In both  
309 cases, the inclusions likely formed from impact melt of original troilite-pentlandite-like phases.  
310 Nevertheless, further studies will be required to provide unambiguous explanation of the origin  
311 of these enigmatic inclusions.

## 312 **IMPLICATIONS**

313 Recent finds of Fe–Ni sulfide inclusions embedded in Muong Nong-type tektites from the  
314 locality close to the Muong Nong village in Laos represent an important observation constraining  
315 not only the origin of Australasian tektites but also a general behavior of Fe–Ni–S system under

316 extreme conditions. In addition, applied methodologies showed their importance and limitations  
317 in identifying such small objects like these inclusions.

- 318 • This is the first reported occurrence of this mineral close to ideal end-member  
319 composition and the first ever occurrence in terrestrial materials.
- 320 • Electron back scatter diffraction proved its indispensability in identification of small  
321 volumes of material; the structural identity of the Fe–Ni sulfide occurring as segments or  
322 patches within the spherical inclusions has been confirmed by unambiguous matching of  
323 the EBSP to the structure of shenzhuangite determined by Bindi and Xie (2018).  
324 Nevertheless, the structures displaying subtle variance among their crystal structures may  
325 pose significant limitation on the use of the technique. In particular, EBSD study could  
326 not unambiguously resolve whether iron monosulfide associated with shenzhuangite is a  
327 higher-order polytype of pyrrhotite or troilite (*2H* polytype).
- 328 • Raman spectrum of shenzhuangite display considerable differences in relative intensities  
329 in comparison to isostructural natural chalcopyrite as well synthetic chalcopyrite-based  
330 phases. Next to variance in intensities, also some shifts of the band positions were  
331 observed. Particularly, intensity of the band, which is tentatively ascribed to the Raman  
332 modes of  $B_2$  and  $E$  symmetries and involves Ni displacements, increases substantially. On  
333 the other hand, the intensity of band expected to represent the  $A_1$  Raman mode decreases  
334 markedly. These features are obviously related to the coupled substitution of monovalent  
335 copper by divalent nickel and ferric by ferrous iron and expectable changes in electronic  
336 configurations around the individual ions. Thus, the Raman spectroscopy provides a  
337 useful tool to uncover such effects though they cannot be quantitatively constrained  
338 solely from the Raman data.

- 339       • Pyrrhotite nickel enrichment observed in the analyses reaches up to ~10 at% and is not  
340       corroborated by the results of published experimental phase relations studies within the  
341       Fe–Ni–S system. Consequently, the elevated nickel content represent an analytical  
342       artefact and must be attributed to either contamination from coexisting shenzhuangite or  
343       extremely fine inclusions of not yet identified Ni-rich phase intergrown with Ni-free  
344       pyrrhotite/troilite.
- 345       • Of general importance is the chemical composition of the phase in inclusions, which is  
346       close to ideal NiFeS<sub>2</sub> stoichiometry. Such a composition is not consistent with any stable  
347       phase in the Fe–Ni–S system up to melting temperature. Consequently, this indicates  
348       specific conditions under which this mineral formed. Available data, however, do not  
349       provide unambiguous clue to determine whether the phase association consisting of  
350       shenzhuangite and pyrrhotite/troilite formed from sort of a superheated melt generated  
351       during and shortly after an impact from tektite parent sediments or if it may be  
352       considered an indicator of meteoritic component trapped in tektite glass. Further study  
353       aiming to find and characterize additional inclusions is required to shed light on this  
354       issue.

## 355    **ACKNOWLEDGMENTS**

356    This research was funded by the Czech Science Foundation Project No. 17-27099S and was  
357    conducted with institutional support RVO 67985831 of the Institute of Geology of the Czech  
358    Academy of Sciences. We highly appreciated the reviews by C. Koeberl and two anonymous  
359    reviewers, which helped to improve the early version of the manuscript.

360

361

362

363 **REFERENCES**

364 Artus, L., Pujol, J., Pascual, J., and Camassel, J. (1990) Lattice dynamics of AgGaSe<sub>2</sub>. II.

365 Theoretical aspects. *Physical Review B*, 41, 5727–5734.

366 Artús, L., Pascual, J., Pujol, J., Camassel, J., and Feigelson, R.S. (1991) Vibrational properties of

367 CdGeP<sub>2</sub>. *Physical Review B*, 43, 2088–2096.

368 Barnes, S.J., Mungall, J.E., Le Vaillant, M., Godel, B., Leshner, C.M., Holwell, D., Lightfoot,

369 P.C., Krivolutszkaya, N., and Wei, B. (2017) Sulfide-silicate textures in magmatic Ni-Cu-

370 PGE sulfide ore deposits: disseminated and net-textured ores. *American Mineralogist*, 102,

371 473–506.

372 Bergerhoff, G., and Brown, I.D. (1987) Crystallographic Databases. In F.H. Allen, G.

373 Bergerhoff, and R. Sievers, Eds., *Crystallographic Databases*. International Union of

374 Crystallography, Chester.

375 Bindi, L., and Xie, X. (2018) Shenzhuangite, NiFeS<sub>2</sub>, the Ni-analogue of chalcopyrite from the

376 Suizhou L6 chondrite. *European Journal of Mineralogy*, 30, 165–169.

377 Boekema, C., Krupski, A.M., Varasteh, M., Parvin, K., van Til, F., van der Woude, F., and

378 Sawatzky, G.A. (2004) Cu and Fe valence states in CuFeS<sub>2</sub>. *Journal of Magnetism and*

379 *Magnetic Materials*, 272–276, 559–561.

380 Brett, R. (1967) Metallic spherules in impactite and tektite glasses. *The American Mineralogist*,

381 52, 721–733.

382 Buzatu, A., Buzgar, N., Damian, G., Vasilache, V., and Apopei, A.I. (2013) The determination

383 of the Fe content in natural sphalerites by means of Raman spectroscopy. *Vibrational*

- 384 Spectroscopy, 68, 220–224.
- 385 Camassel, J., Artus, L., and Pascual, J. (1990) Lattice dynamics of AgGaSe<sub>2</sub>. I. Experiment.  
386 Physical Review B, 41, 5717–5726.
- 387 Cavosie, A.J., Timms, N.E., Erickson, T.M., and Koeberl, C. (2018) New clues from Earth's  
388 most elusive impact crater: Evidence of reidite in Australasian tektites from Thailand.  
389 Geology, 46, 203–206.
- 390 Chao, E.C.T., Adler, I., Dwornik, E.J., and Littler, J. (1962) Metallic spherules in tektites from  
391 Isabela, Philippine Islands. Science, 135, 97–98.
- 392 Chao, E.C.T., Dwornik, E.J., and Litter, J. (1964) New data on the nickel-iron spherules from  
393 Southeast Asian tektites and their implications. Geochimica et Cosmochimica Acta, 28,  
394 971–980.
- 395 Chao, E.C.T., Dwornik, E.J., and Merrill, C.W. (1966) Nickel-iron spherules from Aouelloul  
396 glass. Science, 154, 759–765.
- 397 El Goresy, A. (1966) Metallic spherules in Bosumtwi crater glasses. Earth and Planetary Science  
398 Letters, 1, 23–24.
- 399 Folco, L., Glass, B.P., D'Orazio, M., and Rochette, P. (2018) Australasian microtektites:  
400 Impactor identification using Cr, Co and Ni ratios. Geochimica et Cosmochimica Acta, 222,  
401 550–568.
- 402 Ganapathy, R., and Larimer, J.W. (1983) Nickel-iron spherules in tektites: non-meteoritic in  
403 origin. Earth and Planetary Science Letters, 65, 225–228.
- 404 Glass, B.P., and Barlow, R.A. (1979) Mineral inclusions in Muong Nong-type indochinites:  
405 Implications concerning parent material and process of formation. Meteoritics, 14, 55–67.

- 406 Goderis, S., Tagle, R., Fritz, J., Bartoschewitz, R., and Artemieva, N. (2017) On the nature of the  
407 Ni-rich component in splash-form Australasian tektites. *Geochimica et Cosmochimica Acta*,  
408 217, 28–50.
- 409 Goh, S.W., Buckley, A.N., Lamb, R.N., Rosenberg, R.A., and Moran, D. (2006) The oxidation  
410 states of copper and iron in mineral sulfides, and the oxides formed on initial exposure of  
411 chalcopyrite and bornite to air. *Geochimica et Cosmochimica Acta*, 70, 2210–2228.
- 412 Hall, S.R., and Stewart, J.M. (1973) The crystal structure refinement of chalcopyrite,  $\text{CuFeS}_2$ .  
413 *Acta Crystallographica B*, 29, 579–585.
- 414 Huang, W., Zhao, B., Zhu, S., He, Z., Chen, B., and Yu, Y. (2016) Vibrational modes of  
415 chalcopyrite  $\text{CdGeAs}_2$  crystal. *Materials Research Bulletin*, 81, 107–113.
- 416 Jiménez-Sandoval, S., López-Rivera, A., and Irwin, C. (2003) Influence of reduced mass  
417 differences on the Raman spectra of ternary mixed compounds:  $\text{Zn}_{1-x}\text{Fe}_x\text{S}$  and  $\text{Zn}_{1-x}\text{Mn}_x\text{S}$ .  
418 *Physical Review B*, 68, 054303-1–9.
- 419 Jonášová, Š., Ackerman, L., Žák, K., Skála, R., Ďurišová, J., Deutsch, A., and Magna, T. (2016)  
420 Geochemistry of impact glasses and target rocks from the Zhamanshin impact structure,  
421 Kazakhstan: Implications for mixing of target and impactor matter. *Geochimica et*  
422 *Cosmochimica Acta*, 190, 239–264.
- 423 Kaminow, I.P., Buehler, E., and Wernick, J.H. (1970) Vibrational modes in  $\text{ZnSiP}_2$ . *Physical*  
424 *Review B*, 2, 960–966.
- 425 Keller-Besrest, F., and Collin, G. (1990) II. Structural aspects of the  $\alpha$  transition in off-  
426 stoichiometric  $\text{Fe}_{1-x}\text{S}$  crystals. *Journal of Solid State Chemistry*, 84, 211–225.
- 427 Kharbish, S. (2007) A Raman spectroscopic investigation of Fe-rich sphalerite: effect of Fe-

- 428 substitution. *Physics and Chemistry of Minerals*, 34, 551–558.
- 429 Kitakaze, A., and Sugaki, K. (2004) The phase relations between  $\text{Fe}_{4.5}\text{Ni}_{4.5}\text{S}_8$  and  $\text{Co}_9\text{S}_8$  in the  
430 system Fe–Ni–Co–S at temperatures from 400°C to 1100°C. *The Canadian Mineralogist*,  
431 42, 17–42.
- 432 Kitakaze, A., Sugaki, A., Itoh, H., and Komatsu, R. (2011) A revision of phase relations in the  
433 system Fe–Ni–S from 650° to 450°C. *The Canadian Mineralogist*, 49, 1687–1710.
- 434 Kitakaze, A., Machida, T., and Komatsu, R. (2016) Phase relations in the Fe-Ni-S system from  
435 875 to 650 °C. *The Canadian Mineralogist*, 54, 1175–1186.
- 436 Klekovkina, V.V., Gainov, R.R., Vagizov, F.G., Dooglav, A.V., Golovanevskiy, V.A., and  
437 Pen'kov, N. (2014) Oxidation and magnetic states of chalcopyrite  $\text{CuFeS}_2$ : A first principles  
438 calculation. *Optics and Spectroscopy*, 116, 885–888.
- 439 Koeberl, C. (1992) Geochemistry and origin of Muong Nong-type tektites. *Geochimica et*  
440 *Cosmochimica Acta*, 56, 1033–1064.
- 441 ——— (2014) The Geochemistry and Cosmochemistry of Impacts. In *Treatise on Geochemistry*  
442 Vol. 2, pp. 73–118. Elsevier Ltd.
- 443 Koschel, W., Sorger, F., and Baars, J. (1975) Optical phonons in I-III-VI<sub>2</sub> compounds. *Journal*  
444 *de Physique Colloques*, 36 (C3), C3-177-C3-181.
- 445 Lafuente, B., Downs, R.T., Yang, H., and Stone, N. (2015) The power of databases: The RRUFF  
446 project, 1-29 p. (T. Armbruster & R.M. Danisi, Eds.) *Highlights in Mineralogical*  
447 *Crystallography*. Berlin.
- 448 Łażewski, J., Neumann, H., and Parlinski, K. (2004) Ab initio characterization of magnetic  
449  $\text{CuFeS}_2$ . *Physical Review B*, 70, 195206-1–7.

- 450 Mintairov, A.M., Sadchikov, N.A., Sauncy, T., Holtz, M., Seryogin, G.A., Nikishin, S.A., and  
451 Temkin, H. (1999) Vibrational Raman and infrared studies of ordering in epitaxial ZnSnP<sub>2</sub>.  
452 Physical Review B, 59, 15197–15207.
- 453 O’Keefe, J.A. (1984) Comments on paper by R. Ganapathy & J.W. Larimer: Nickel-iron  
454 spherules in tektites: non-meteoritic in origin. Journal of Non-Crystalline Solids, 67, 371–  
455 374.
- 456 Ohrendorf, F.W., and Haeuseler, H. (1999a) Lattice dynamics of chalcopyrite type compounds.  
457 Part I. Vibrational frequencies. Crystal Research and Technology, 34, 339–349.
- 458 ——— (1999b) Lattice dynamics of chalcopyrite type compounds. Part II. Calculations in a  
459 short range force field model. Crystal Research and Technology, 34, 351–362.
- 460 Osadchii, E.G., and Gorbaty, Y.E. (2010) Raman spectra and unit cell parameters of sphalerite  
461 solid solutions (Fe<sub>x</sub>Zn<sub>1-x</sub>S). Geochimica et Cosmochimica Acta, 74, 568–573.
- 462 Pascual, J., Pujol, J., Artus, L., and Camassel, J. (1991) Alternating anion-cation bond strengths  
463 in CdGeAs<sub>2</sub>: Application to the family of ternary pnictides. Physical Review B, 43, 9832–  
464 9842.
- 465 Rajamani, V., and Prewitt, C.T. (1975) Thermal expansion of the pentlandite structure. American  
466 Mineralogist, 60, 39–48.
- 467 Skála, R., Jonášová, Š., Žák, K., Ďurišová, J., Brachaniec, T., and Magna, T. (2016) New  
468 constraints on the Polish moldavite finds: A separate sub-strewn field of the central  
469 European tektite field or re-deposited materials? Journal of Geosciences, 61, 171–191.
- 470 van der Ziel, J.P., Meixner, A.E., Kasper, H.M., and Ditzenberger, J.A. (1974) Lattice vibrations  
471 of AgGaS<sub>2</sub>, AgGaSe<sub>2</sub>, and CuGaS<sub>2</sub>. Physical Review B, 9, 4286–4294.

- 472 Vaughan, D.J., and Craig, J.R. (1997) Sulfide ore mineral stabilities, morphologies, and  
473 intergrowth textures. In H.L. Barnes, Ed., *Geochemistry of hydrothermal ore deposits*, pp.  
474 367–434. John Wiley and Sons Inc., New York.
- 475 Weber, I., Böttger, U., Pavlov, S.G., Hübers, H.W., Hiesinger, H., and Jessberger, E.K. (2017)  
476 Laser alteration on iron sulfides under various environmental conditions. *Journal of Raman*  
477 *Spectroscopy*, 48, 1509–1517.
- 478 Wojdyr, M. (2010) Fityk: a general-purpose peak fitting program. *Journal of Applied*  
479 *Crystallography*, 43, 1126–1128.
- 480 Žák, K., Skála, R., Pack, A., Ackerman, L., and Křížová, Š. (2019) Triple oxygen isotope  
481 composition of Australasian tektites. *Meteoritics & Planetary Science*, 1167–1181.
- 482 Zigone, M., Vandevyver, M., and Talwar, D.N. (1981) Raman scattering and local force  
483 variations due to transition-element impurities in zinc-sulfide crystals: Effect of pressure  
484 application. *Physical Review B*, 24, 5763–5778.

485

## 486 **Figure captions**

487 **Figure 1.** Macroscopic appearance of the Australasian tektites hosting the inclusions of  
488 shenzhuangite (a,c,e) and images illustrating textures of individual samples as seen in transmitted  
489 light in thick (~400 μm) polished sections (b,d,f). Note prominent layering and vesiculation in  
490 the samples MN 12 and MN 16.

491 **Figure 2.** Optical micrographs of Muong Nong-type tektite hosting sulfide inclusions illustrating  
492 bubbles, and lechatelierite filaments emphasizing fluidal structure on micrometer scale (a) and  
493 marked macroscopic layering (b). Plane polarized transmitted light.

494 **Figure 3.** Back-scattered electron images of the shenzhuangite-bearing inclusions in the Muong  
495 Nong-type tektite from Laos. Next to shenzhuangite (sh), inclusions contain also troilite (tr). The  
496 inclusions show sharp border towards hosting tektite glass yet in some cases fine protrusions  
497 (ptrs) radiate to a surrounding glass.) Distribution of low-Ni phase within shenzhuangite is  
498 either of patchy (b) or segmented (c) appearance.

499 **Figure 4.** Electron back-scatter diffraction patterns of shenzhuangite (a,c) and corresponding  
500 indexing of Kikuchi bands (b,d).

501 **Figure 5.** The triangular diagram (a) shows the extent of the plot (b) in the Fe-Ni-S system. The  
502 plot (b) illustrates the chemical composition (in at%) of shenzhuangite in spherules enclosed in  
503 Muong Nong-type tektites from Laos (triangles) and the extent of monosulfide solid solution  
504 (mss; gray field); at 1000 °C after Vaughan and Craig (1997). Note that most analyses of  
505 shenzhuangite overlap; the only outlier corresponds to the analysis MN 16 i4b.

506 **Figure 6.** Comparison of Raman spectra of shenzhuangite from the inclusion MN 7 i7,  
507 chalcopyrite and pentlandite. Mutual differences in band intensities between shenzhuangite and  
508 chalcopyrite are due to different occupation of structure sites in them. Pentlandite spectrum is  
509 incompatible with both shenzhuangite and chalcopyrite spectra. The spectrum of shenzhuangite  
510 is shown in pale blue. Below it, individual deconvoluted bands are displayed. Overlain over the  
511 shenzhuangite measured spectrum is the model summed from individual deconvoluted bands  
512 (dark blue line). Below the spectrum, shown in gold, is the difference curve illustrating the match  
513 between modelled and measured data. Spectra of chalcopyrite and pentlandite were taken from  
514 the RRUFF database. Raman scattering intensity is given in arbitrary units (a.u.).

Table 1 Chemical composition (in at%, normalized wt% and apfu) of shenzhuangite domains found in inclusions embedded in Laotian Muong Nong-type tektites determined by EPMA

| Sample | Inclusion | at%   |       |        |        |       | wt%   |       |        |        |       | empirical formula per 4 apfu |       |       |       |       |       |
|--------|-----------|-------|-------|--------|--------|-------|-------|-------|--------|--------|-------|------------------------------|-------|-------|-------|-------|-------|
|        |           | Ni    | Fe    | Cu     | Co     | S     | Ni    | Fe    | Cu     | Co     | S     | Total                        | Ni    | Fe    | Cu    | Co    | S     |
| MN 7   | i7b       | 30.18 | 21.86 | b.d.l. | 0.50   | 47.46 | 38.99 | 26.87 | b.d.l. | 0.65   | 33.49 | 100                          | 1.207 | 0.875 |       | 0.020 | 1.898 |
|        | i15b      | 28.29 | 23.80 | 0.37   | 0.75   | 46.75 | 36.45 | 29.17 | 0.51   | 0.97   | 32.90 | 100                          | 1.132 | 0.952 | 0.015 | 0.030 | 1.871 |
|        | i15c      | 28.63 | 23.12 | b.d.l. | 0.74   | 47.39 | 37.06 | 28.47 | b.d.l. | 0.97   | 33.50 | 100                          | 1.146 | 0.926 |       | 0.030 | 1.898 |
| MN 12  | i3a*      | 29.12 | 21.18 | b.d.l. | b.d.l. | 49.69 | 38.11 | 26.37 | b.d.l. | b.d.l. | 35.52 | 100                          | 1.165 | 0.847 |       |       | 1.988 |
| MN 13  | i1c       | 28.57 | 22.29 | b.d.l. | 0.94   | 48.14 | 37.10 | 27.53 | b.d.l. | 1.23   | 34.14 | 100                          | 1.143 | 0.892 |       | 0.038 | 1.927 |
| MN 16  | i4b       | 25.16 | 24.93 | 0.39   | 1.45   | 48.02 | 32.68 | 30.81 | 0.55   | 1.89   | 34.06 | 100                          | 1.007 | 0.998 | 0.016 | 0.058 | 1.922 |

a-c single point analyses in particular inclusion

b.d.l. below detection limit

\* low total is due to uneven surface of the inclusion

Table 2 Band positions, widths and intensities in Raman spectrum of shenzhuangite

| No.                         | 1      | 2      | 3      | 4      | 5                 | 6      | 7      | 8      | 9               | 10     | 11    | 12     | 13     |
|-----------------------------|--------|--------|--------|--------|-------------------|--------|--------|--------|-----------------|--------|-------|--------|--------|
| $\omega$ , $\text{cm}^{-1}$ | 154.35 | 170.41 | 198.94 | 222.44 | 254.08            | 287.79 | 307.98 | 328.14 | 370.49          | 389.62 | 406.7 | 672.91 | 720.79 |
| FWHM, $\text{cm}^{-1}$      | 7.04   | 20.35  | 24.58  | 33.9   | 24.84             | 36.96  | 31.76  | 43.25  | 33.34           | 20.73  | 12.14 | 21.83  | 15.55  |
| Height, a.u.                | 7.4    | 15.1   | 2.9    | 9.5    | 16.7              | 23.8   | 14.1   | 16.6   | 100             | 17.9   | 7.5   | 10.3   | 3.2    |
| Area, a.u.                  | 1.6    | 9.3    | 2.1    | 8.6    | 12.5              | 26.4   | 13.5   | 21.6   | 100             | 11.2   | 2.7   | 10.8   | 2.5    |
| Tentative assignment        | ext    | E(L)   | B1     | ext    | B2(T,L)<br>E(T,L) | A1     | comb   | E(T,L) | E(T,L)<br>B2(T) | B2(L)  | comb  | comb   | comb   |

Notes: ext = external modes; comb = combination bands / overtones

$\omega$  ... band position

FWHM ... band full width in half maximum

Height ... band height

Area ... band intensity

Tentative assignment ... assignment of bands to vibrational modes

# Figure 1

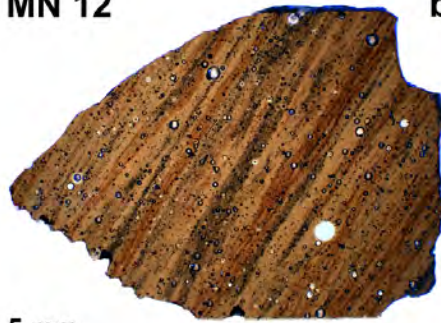
MN 12



2 cm

a

MN 12



5 mm

b

MN 13



2 cm

c

MN 13



5 mm

d

MN 16



2 cm

e

MN 16



5 mm

f

**Figure 2**

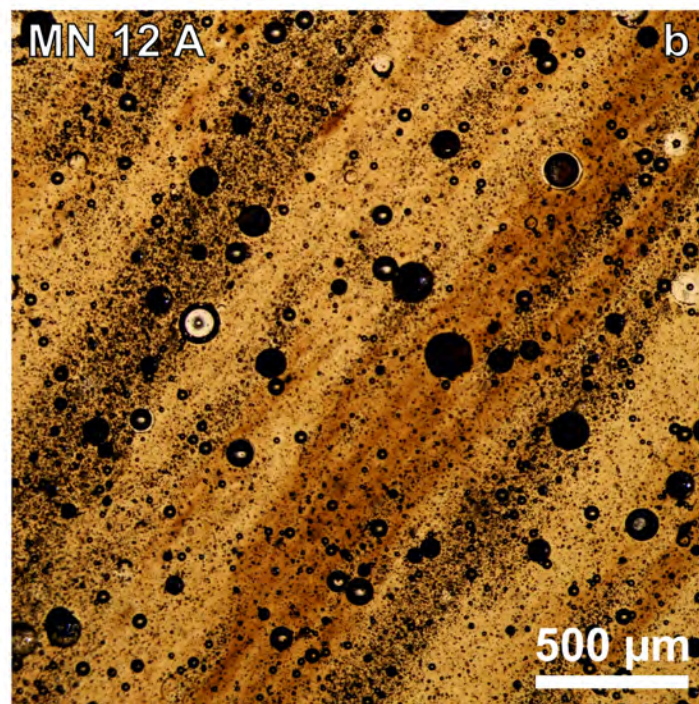
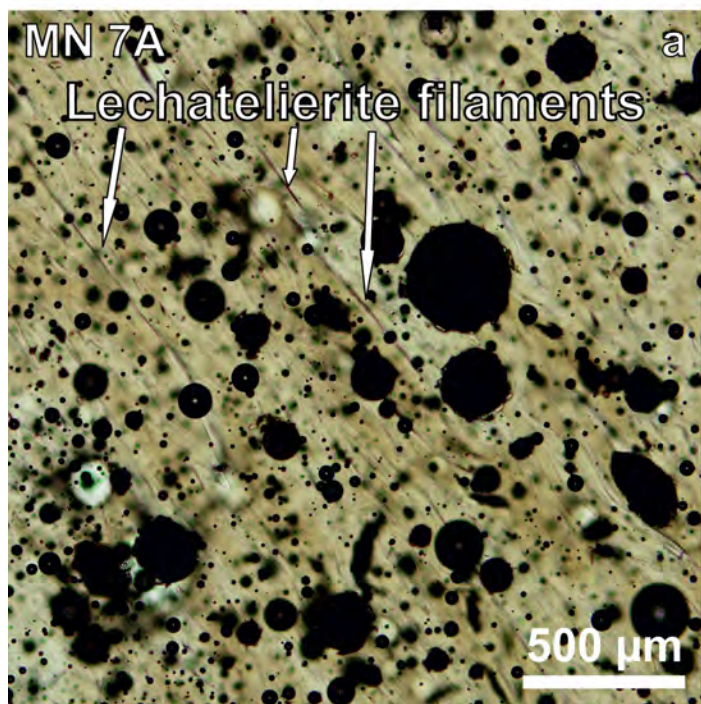


Figure 3

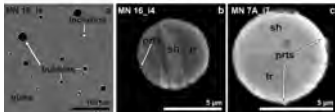


Figure 4

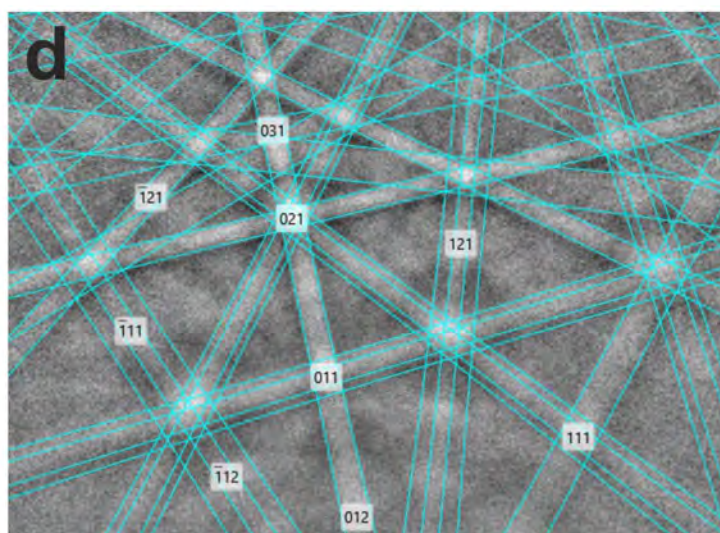
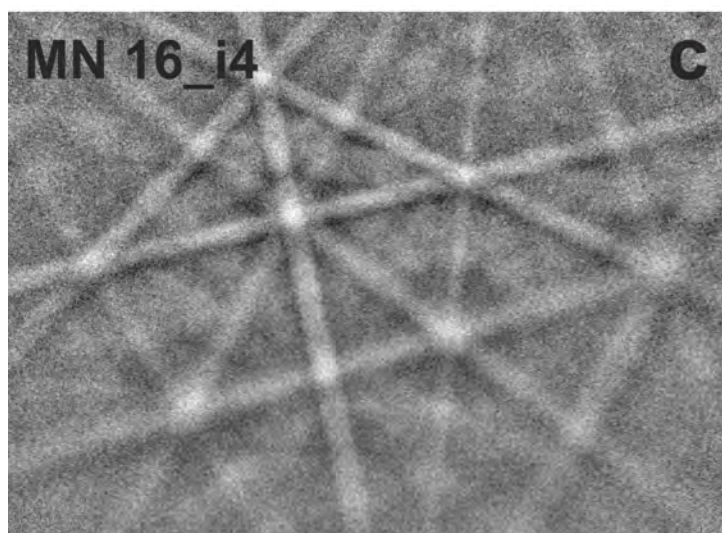
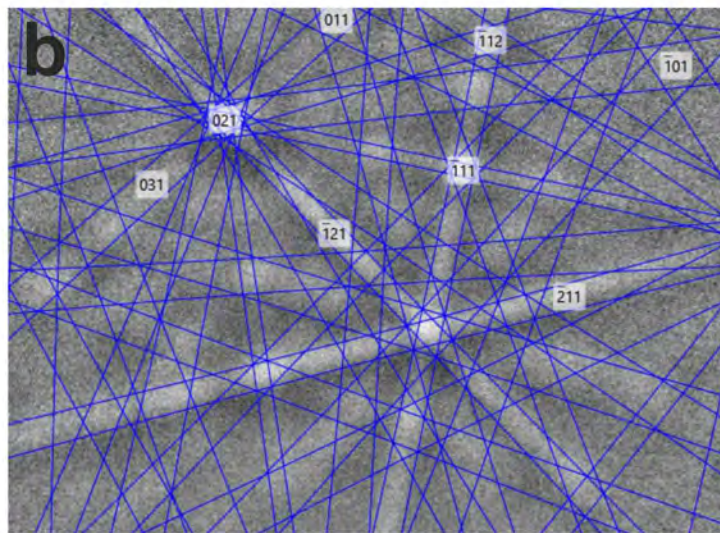
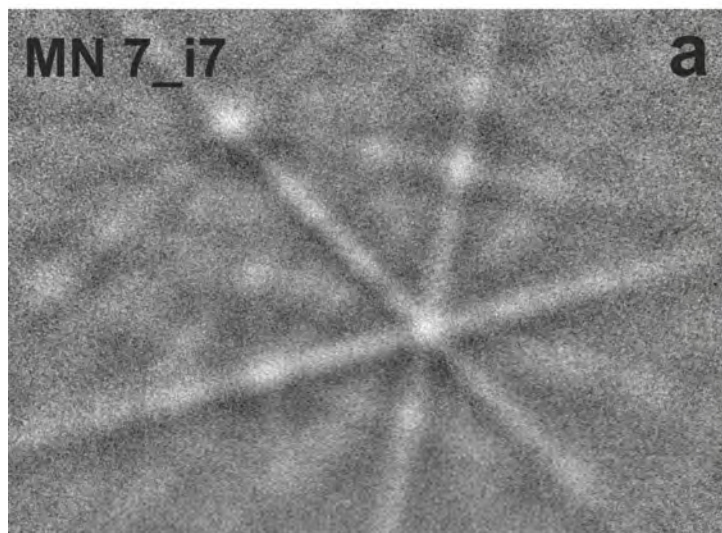
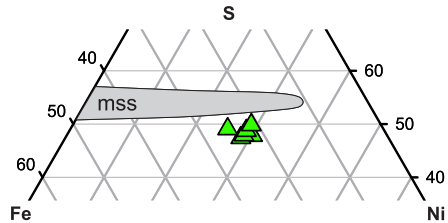
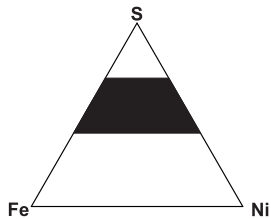


Figure 5



# Figure 6

